ACS OMEGA

Open Access

http://pubs.acs.org/journal/acsodf

Article

Geomimetic Thermosynthesis in Heterogeneous Structural Complexes of In Situ Growing Imine-Based COF on MXene for Enhanced Sodium Ion Storage

Xiping Luo,‖ Mfitumucunguzi Steven,‖ Zi-Li Feng,‖ Yu-Xuan Wang, Xue-Juan Yang, Lu Zheng,* Chuanwei Zhi,* and Chaofei Guo*

Cite This: *ACS Omega* 2025, 10, 16952−16961

Read Online

ACCESS | Metrics & More | Article Recommendations | Supporting Information

ABSTRACT: Covalent organic frameworks (COFs) have gained significant attention as next-generation electrode materials for energy storage, owing to their chemical versatility, ecofriendliness, and cost-effectiveness. However, their practical application in energy storage systems is hindered by challenges such as insufficient exposure of functional groups for sodium storage and poor ion/electron transport kinetics. In this work, we developed an organic−inorganic heterojunction structure by in situ growth of an imine-based COF on the surface of MXene, which was employed as an anode material for sodium-ion batteries. This heterojunction design enhances sodium ion and electron transport, while the porous COF layer maximizes the exposure of active sites. In situ FT-IR and Raman spectroscopy analyses reveal that the C═N and C═C functional groups in the COF@D-$Ti_3C_2T_x$ electrode enable reversible sodium-ion storage. Furthermore, the flexible hydrogen bonds between the COF and MXene layers effectively mitigate volume expansion during cycling, improving the structural stability and long-term cycling performance. As a result, the COF@D-$Ti_3C_2T_x$ composite electrode delivers a remarkable reversible capacity of 401.6 mA h g^{-1} after 300 cycles at 0.1 C. This work not only introduces a novel synthesis strategy for imine-based COFs but also explores sodium−active reaction units and organic−inorganic heterojunction designs, offering new insights for advancing rechargeable battery technologies.

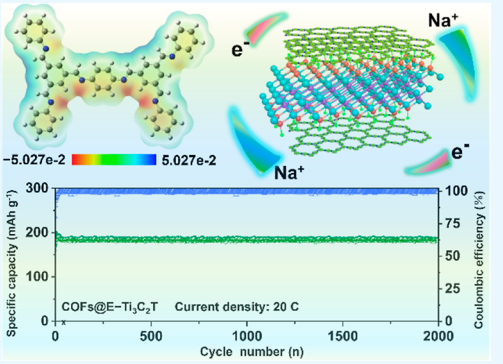

1. INTRODUCTION

The rapid expansion of electric vehicles (EVs) and smart grids has intensified the demand for high-energy-density sodium-ion batteries (SIBs), which are considered a promising alternative to lithium−ion batteries due to the abundance and low cost of sodium resources.[1,2] Rechargeable SIBs have found widespread use in applications such as EVs, portable electronics, and large-scale energy storage systems. However, the theoretical capacity of commercially available graphite anodes, which is limited to 372 mA h g^{-1}, has already been reached, creating a significant bottleneck for further advancements in energy storage technology.[3−5] Thus, the development of electrode materials with superior electrochemical performance is urgently needed.[6]

Covalent organic framework (COF), first reported in 2005, are porous and 2D materials connected by covalent bonds.[7,8] Their extended π-conjugated structures, permanent porosity, large specific surface areas, high physical and chemical stability, and abundance of active sites have enabled their application in supercapacitors, catalysis, gas storage, and sensing technologies.[9−11] These characteristics also make COFs highly attractive as electrode materials for SIBs, as their tunable structures and functional groups can potentially enhance sodium-ion storage capabilities.[12,13] However, the practical application of COFs in batteries is hindered by their inherently poor electrical conductivity and the difficulty in fully activating redox-active sites during electrochemical processes.[14−16] To address these challenges, various strategies have been explored, including the integration of COFs with conductive polymers, carbon nanotubes, and graphene, which have shown promise in improving conductivity and increasing the accessibility of active reaction sites.[17−19] Another effective approach involves growing the COF directly on conductive substrates, which leverages interfacial interactions to achieve fast ion and charge transfer.

MXenes, a family of 2D materials discovered in 2011, have emerged as highly promising candidates for energy storage applications due to their unique properties. With the general formula $M_{n+1}X_nT_x$ (n = 1−3), where M represents transition metals, X represents carbon or nitrogen, and T denotes surface functional groups such as −O, −OH, or −F, MXenes exhibit exceptional electrical conductivity, low sodium-ion diffusion

Received: February 17, 2025
Revised: April 6, 2025
Accepted: April 9, 2025
Published: April 14, 2025

barriers, and tunable surface chemistry.[20,21] These properties make MXenes particularly suitable for energy storage and conversion applications, as they can facilitate efficient charge transfer and ion diffusion while providing a stable platform for material integration.[22,23]

Building on recent advancements in the hydrothermal synthesis of polyimide crystals, we developed a highly crystalline imine-based COF via geometric heating without the use of catalysts or toxic solvents. Imine bonds, which enhance chemical stability, were utilized as covalent linkages in the synthesis. These imine-based COF subsequently in situ grown on the $Ti_3C_2T_x$ MXene, capitalizing on the material's excellent charge mobility and tunable surface chemistry. The hydrogen bonding between MXene and the COF maximizes the exposure of active sites in the COF, significantly improving their electrochemical performance. This innovative heterojunction structure demonstrates remarkable capabilities, including fast sodium-ion conduction, efficient charge transfer, and substantial potential for high-performance energy storage applications, paving the way for the development of advanced battery technologies.

In this work, we successfully synthesized imine-based COF through a green and sustainable approach and constructed a 2D sandwich-like heterojunction by in situ growth of COF on MXene. Comprehensive in situ FT-IR and Raman spectroscopy analyses at various discharging/charging voltages confirmed that the heterojunction structure significantly enhances the exposure of functional groups for sodium storage and facilitates efficient charge transfer. Furthermore, the flexible hydrogen bonds formed between the COF and MXene layers not only improve structural stability but also effectively mitigate volume expansion during cycling, ensuring exceptional long-term cycling stability. The COF@D-$Ti_3C_2T_x$ electrode exhibited outstanding electrochemical performance, delivering a reversible capacity of 401.6 mA h g^{-1} after 300 cycles at 0.1 C. Remarkably, the COF@D-$Ti_3C_2T_x$ electrode demonstrated exceptional stability at ultrahigh current densities (20 C), maintaining consistent performance over 2000 cycles, highlighting its superior rate capability. Additionally, the capacity contribution of the COF component closely approached its theoretical capacity based on its weight percentage in the composite. This innovative synthesis strategy and its promising results provide a new pathway for designing high-performance imine-based COF materials as advanced electrodes for SIBs, paving the way for next-generation energy storage technologies.

2. EXPERIMENTAL SECTION

2.1. Materials. Hydrofluoric acid (HF, ≥40.0%), *N*,*N*-dimethylformamide (DMF, AR, ≥99.5%), tetrahydrofuran (THF) (AR, ≥99.0%), ethanol (AR, ≥95.0%), potassium hydroxide (KOH, ≥85.0%), acetone (CP, 99.5%), 1,4-diaminobenzene (1,4-DAB, ≥99.0%), and 1,3,5-benzenetricarboxaldehyde (1,3,5-BTC, 99.0%) were purchased from Sinopharm Chemical. 1,3-dioxolane/1,2-dimethoxy-ethane (DOL/DME, 1:1, v/v) was purchased from DoDoChem. TBAP (98%) was purchased from Yanshen Technology Co., Ltd. Suzhou Beike NanoTechnology Co., Ltd. provided Ti_3AlC_2.

2.2. Synthesis of Delaminated MXene (D-$Ti_3C_2T_x$). Typically, Ti_3AlC_2 powder was slowly added to HF (≥40.0%), and the mixture was stirred for 48 h at room temperature. The mixture was centrifuged and washed with deionized water and ethanol until the supernatants pH turned 6. The obtained $Ti_3C_2T_x$ MXene was then sonicated in a KOH solution (0.1 mol L^{-1}) for 6 h to obtain the exfoliated MXene sheets. The mixture was centrifuged at 3500 rpm for 10 min, and the upper dispersion was collected and vacuum-dried to obtain D-$Ti_3C_2T_x$ MXene nanosheets.

2.3. Synthesis of Imine-Based COF and Imine-Based D-$Ti_3C_2T_x$. Initially, 1,4-DAB (27 mg, 0.15 mmol) and 1,3,5-BTC (24 mg, 0.15 mmol) were dissolved in 1.5 mL of 1,4-dioxane. Subsequently, 0.2 mL of 3.0 mol/L aqueous acetic acid was added to the resulting suspension. The mixture was then transferred to a 25 mL Schlenk bottle, which was purged with nitrogen and sealed. The reaction was carried out at 120 °C for 48 h. The precipitate was sequentially washed with THF and *N*,*N*-DMF, followed by Soxhlet extraction using THF. The final product was dried overnight under a vacuum at 60 °C, yielding a yellow powder of the COF. For the synthesis of COF@MXene, the same procedure was followed, with the addition of 8 mg of MXene at the initial step.

2.4. Materials Characterizations. Instruments for characterizing the structure and morphology of composite materials: (1) X-ray diffractometer (Bruker D8 ADVANCE) and (2) scanning electron microscope (SEM, JSM-6700F; TEM, JEM-2010F). X-ray photoelectron spectrometry (PHI ESCA-5000C) determined the composites surface composition. The samples specific surface area and pore size were obtained using a Micromeritics analyzer (ASAP 2460). A Nicolet iS50 FT-IR instrument was used to obtain the IR spectra of the samples.

2.5. Electrochemical Tests. The active material was mixed with bamboo-derived carbon and binder (cellulose sodium, CMC) in a mass ratio of 70:18:12 to prepare the working electrode. The electrochemical properties of the working electrode were characterized in a CR2032 button cell, which was assembled in an argon-filled glovebox. Sodium foil was used as the counter electrode, and a mixture of 1 M $NaClO_4$ in vinyl carbonate/diethyl carbonate solvent (EC/DEC = 1:1, v/v) was used as the electrolyte for the SIBs. The charge/discharge performance was examined on a LAND-CT2001 system. Cyclic voltammetry (CV 0.1 mV s^{-1}) and electrochemical impedance spectroscopy (EIS) tests (100 kHz to 0.01 Hz, 5 mV) were performed on a CHI660D electrochemical workstation.

2.6. In Situ FT-IR Measurement. For in situ FT-IR measurements, a foamed nickel working electrode was used with a custom battery testing device featuring a diamond window. The setup included a diamond window base, a titanium-wire-integrated sealing ring, a cell container, and a stainless steel component with electrode tabs. During charging and discharging, infrared light passed through the diamond window to monitor the electrode functional groups. The Nicolet iS50 FT-IR spectrometer was connected to the LAND CT2001 battery test system to form the in situ FT-IR system. Spectrograms were collected every 15 min during cycling, with the initial electrode state compared to the background for analysis.

2.7. In Situ Raman Measurement. Raman spectroscopy was performed by using a Renishaw Plus laser Raman spectrometer (785 nm wavelength, 3 mW power). The active electrode material was applied to a copper mesh and placed in an in situ analytical sodium battery test device. The Raman laser passed through the quartz glass window of the device, which was linked to a LAND-CT2001C test system for electrochemical measurements.

2.8. Computational Methods. All data in this study were calculated with the Gaussian 16 software package and were optimized at the B3LYP level of density functional theory.

https://doi.org/10.1021/acsomega.5c01505
ACS Omega 2025, 10, 16952−16961

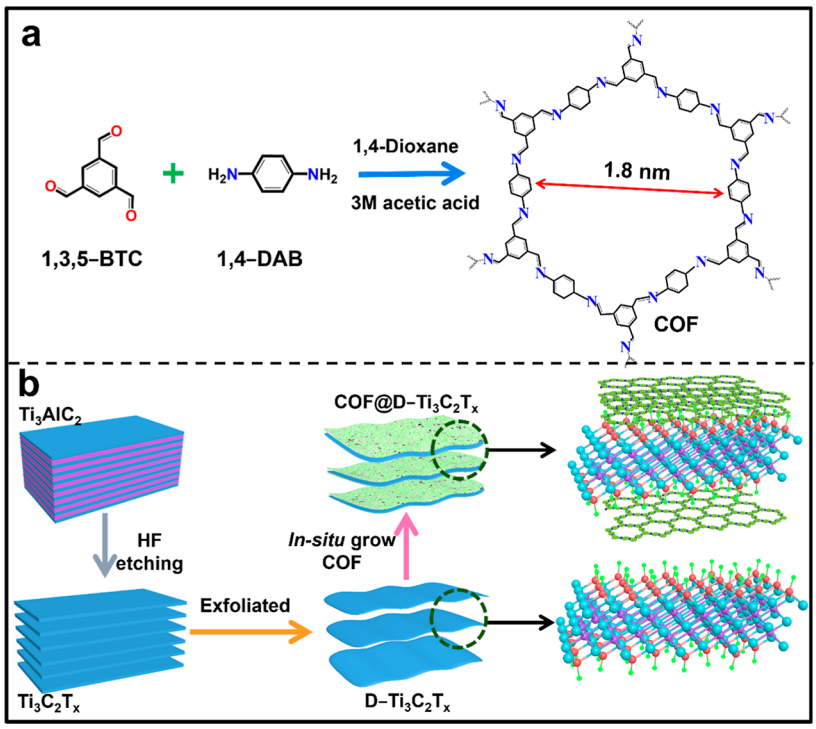

Figure 1. (a) Illustration of the synthesis of COF. (b) Schematic illustration on the fabrication of D-$Ti_3C_2T_x$ MXene nanosheets and the growth of COF@D-$Ti_3C_2T_x$ heterostructure.

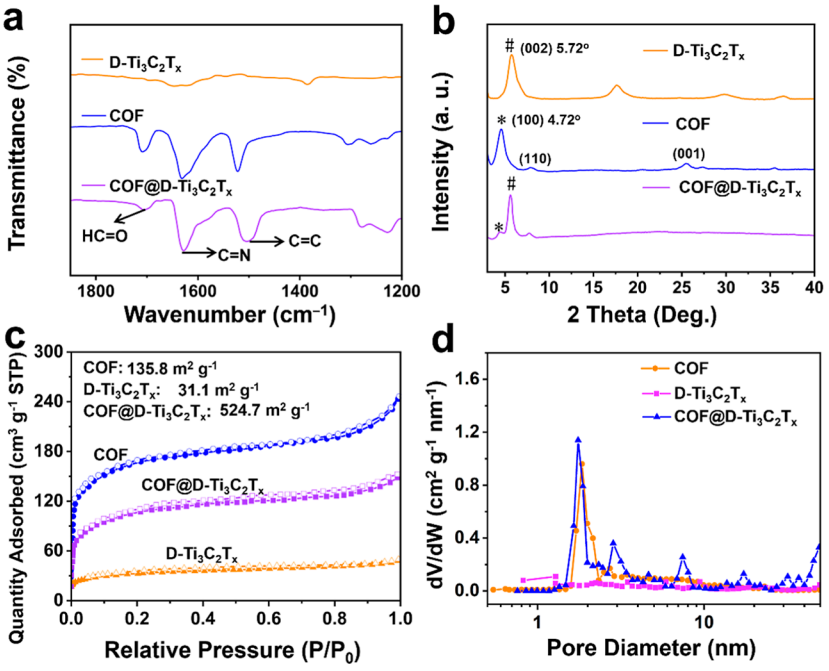

Figure 2. (a) FT-IR spectra of COF, D-$Ti_3C_2T_x$, and COF@D-$Ti_3C_2T_x$. (b) XRD spectra of COF, D-$Ti_3C_2T_x$, and COF@D-$Ti_3C_2T_x$. (c) N_2 adsorption−desorption isotherms curves of COF, D-$Ti_3C_2T_x$, and COF@D-$Ti_3C_2T_x$. (d) The pore size distribution of COF@D-$Ti_3C_2T_x$.

3. RESULTS AND DISCUSSION

3.1. Materials Preparation and Characterization. As illustrated in Figure 1a, the COF was synthesized through a condensation reaction between 1,3,5-BTC and 1,4-DAB under hydrothermal conditions, yielding a yellow powder (Figure S1). The synthesis strategy for the COF@D-$Ti_3C_2T_x$ heterostructures is illustrated in Figure 1b. First, the Al layer in Ti_3AlC_2 was etched by using HF to produce Ti_3C_2 MXene, which was subsequently exfoliated in a KOH solution to generate hydroxyl-functionalized $Ti_3C_2T_x$ nanosheets. In alkaline environments, such as KOH solutions, halogen functional groups like −F or −Cl on the MXene surface are often replaced by −OH groups, increasing the surface hydroxyl (−OH) content. High-resolution Ti 2p XPS spectra of the COF@D-$Ti_3C_2T_x$ heterostructure revealed three doublets corresponding to the Ti $2p_{3/2}$ and Ti $2p_{1/2}$ states. The Ti $2p_{3/2}$ peaks at 459.9, 457.0,

https://doi.org/10.1021/acsomega.5c01505
ACS Omega 2025, 10, 16952−16961

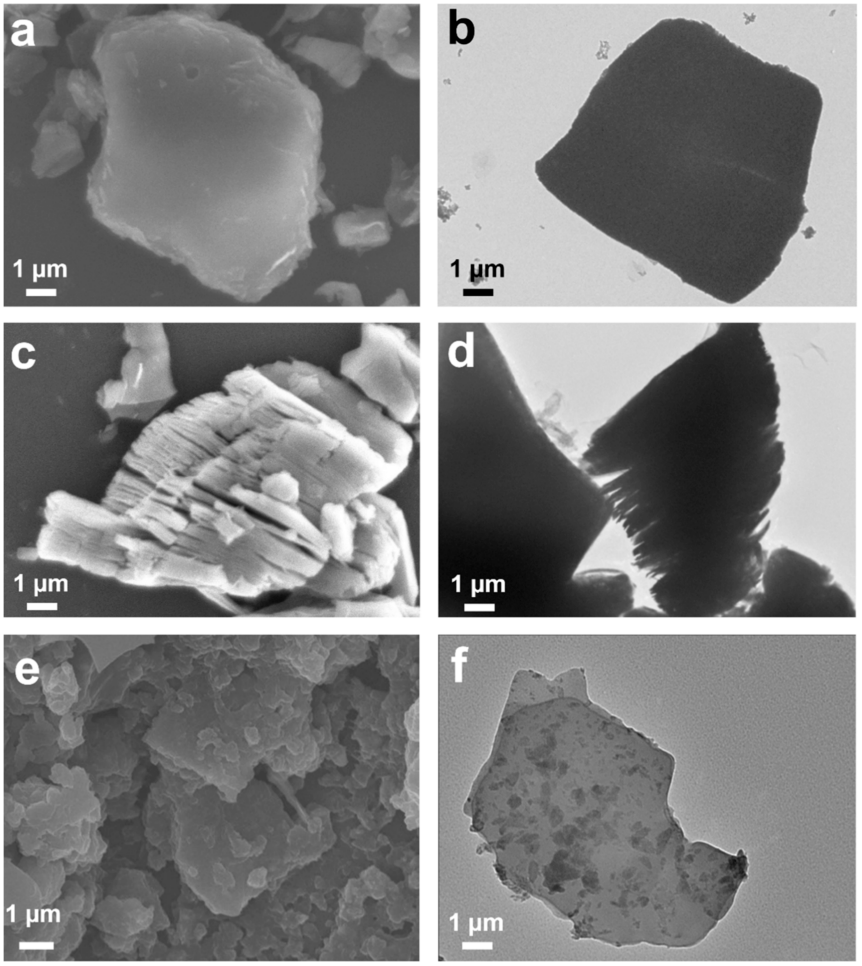

Figure 3. (a) SEM images of Ti_3AlC_2. (b) TEM images of Ti_3AlC_2. (c) SEM images of $Ti_3C_2T_x$. (d) TEM images of $Ti_3C_2T_x$. (e) SEM image of COF@D-$Ti_3C_2T_x$. (f) TEM images of COF@D-$Ti_3C_2T_x$.

and 455.3 eV were assigned to Ti−OH, Ti(II), and Ti−C species, respectively. The significant presence of Ti−OH in the Ti 2p spectrum indicated that the MXene surface was predominantly functionalized with hydroxyl (−OH) groups (Figure S2). Subsequently, the MXene nanosheets were introduced into the COF synthesis in a 1,4-dioxane/acetic acid solution, enabling −OH groups on MXene to form hydrogen bonds with −N groups and facilitating the growth of the COF nanosheets on the $Ti_3C_2T_x$ surface. The FT-IR spectrum of COF exhibited a distinct peak at 1629 cm^{-1}, corresponding to C═N vibrations and confirming the formation of imine bonds during the condensation reaction (Figure 2a).[24,25] The characteristic peak at 1509 cm^{-1} can be attributed to aromatic C═C vibrations of benzene rings, while the minor peak at 1710 cm^{-1} indicates terminal aldehydes.[26] Notably, the characteristic peaks of the COF can be preserved after its in situ growth on MXene, confirming the structural maintenance and stability through hydrogen bonding in the COF@D-$Ti_3C_2T_x$ heterostructures.

The XRD pattern displays a prominent diffraction peak at 4.72° and a weaker, broader peak at 25.46°, indicating an AA stacking pattern of COF (Figure 2b).[27] For D-$Ti_3C_2T_x$, a typical diffraction peak at 5.74° corresponding to the (002) lattice can be detected.[28,29] In the XRD patterns of the COF@D-$Ti_3C_2T_x$ heterostructure, characteristic peaks from both the COF and D-$Ti_3C_2T_x$ can be observed, confirming the successful formation of the composite. Additionally, the (002) peak of COF@D-$Ti_3C_2T_x$ shifts to a lower angle of 5.52°, suggesting slight expansion of the MXene interlayer spacing due to structural accumulation and binding effects between the COF and MXene layers. The COF exhibits type-IV isotherm adsorption/desorption curves (Figure 2c) with sharp nitrogen adsorption below P/P_0 = 0.05, indicating the presence of micropores. The absence of hysteresis in the curves suggests a reversible adsorption/desorption mechanism. The Brunauer−Emmett−Teller (BET) surface area of the COF comes out to be 135.8 m^2 g^{-1}, with a pore size distribution of ∼1.6−1.8 nm. For the COF@D-$Ti_3C_2T_x$ composite, a significantly higher BET surface area of 524.7 m^2 g^{-1} and a similar pore size distribution (∼1.7 nm) can be observed, indicating that the in situ growth of the COF on the MXene surface can expose more pores and increase the overall surface area.

Thermogravimetric analysis (Figure S3) reveals that D-$Ti_3C_2T_x$ exhibits good thermal stability with weight loss primarily attributed to the removal of surface-adsorbed −OH groups. In contrast, COF demonstrates poor thermal stability with a decomposition temperature of approximately 330 °C. Notably, the decomposition temperature of COF@D-$Ti_3C_2T_x$ increased to 410 °C due to the numerous hydrogen bonds between the COF and MXene. It further suggests the enhancing thermal stability of the COF@D-$Ti_3C_2T_x$ heterostructures and the hydrogen binding between them. SEM and TEM images of

https://doi.org/10.1021/acsomega.5c01505
ACS Omega 2025, 10, 16952−16961

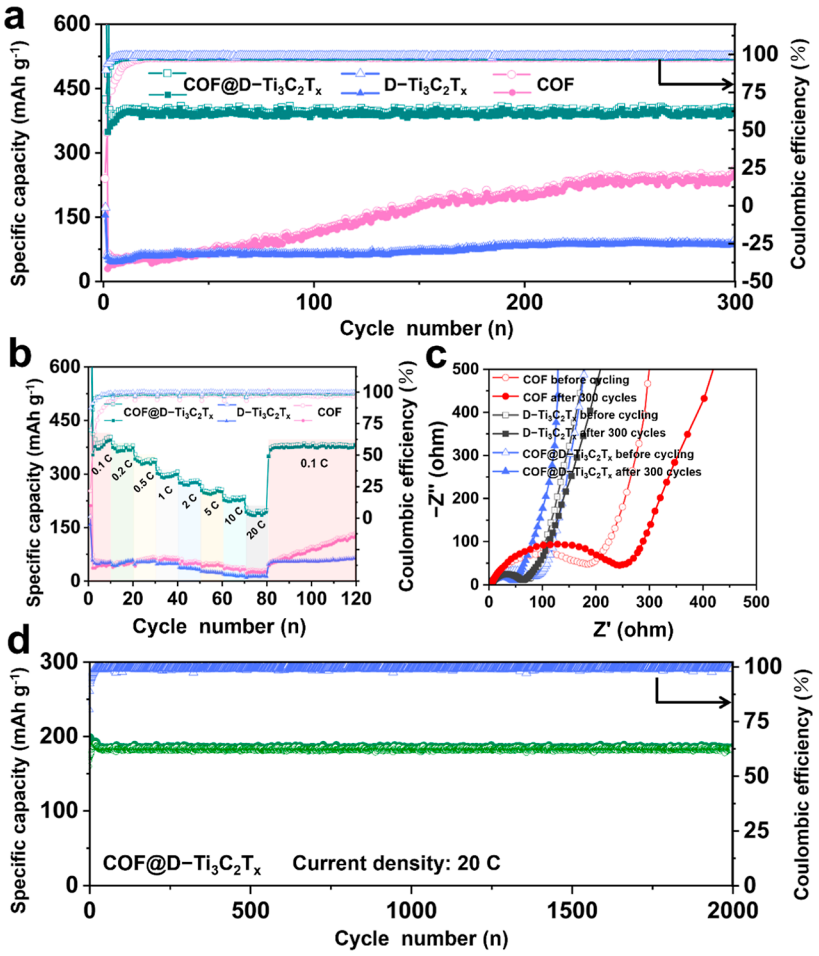

Figure 4. (a) Cycle performance of COF, D-$Ti_3C_2T_x$, and COF@D-$Ti_3C_2T_x$ at 0.1 C. (b) Rate capabilities of COF, D-$Ti_3C_2T_x$, and COF@D-$Ti_3C_2T_x$ at different current rates from 0.1 to 20 C. (c) EIS measurements of the COF, D-$Ti_3C_2T_x$, and COF@D-$Ti_3C_2T_x$. (d) Cycling performance of COF@D-$Ti_3C_2T_x$ at 20 C.

Ti_3AlC_2 show the typical layered structure of the MAX phases (Figure 3a,b). After HF etching, $Ti_3C_2T_x$ exhibits a multilayer, accordion-like 2D structure (Figure 3c,d). Exfoliation of $Ti_3C_2T_x$ by sonication in KOH produces smooth, sheet-like D-$Ti_3C_2T_x$ nanosheets (Figure S4a). In addition, the COF exhibits a 2D nanosheet stacking morphology (Figure S4b). SEM and TEM images of the COF@D-$Ti_3C_2T_x$ composite show a rough surface morphology (Figure 3e,f), suggesting the in situ growth of COF nanosheets on the D-$Ti_3C_2T_x$ surface.

3.2. Electrochemical Performances. The electrochemical performances of COF@D-$Ti_3C_2T_x$, pristine COF, and D-$Ti_3C_2T_x$ MXene as anode materials for SIBs were systematically evaluated. The theoretical capacity of the COF was calculated to be 1830 mA h g^{-1} according to the formula: $Q = nF/3.6M$, where n (the number of electron transferred per molecule) is determined to be 14 (accounting for one sodium ion per C═N group and six per benzene ring), F represents the Faraday constant (96 500 C mol^{-1}), M stands for the molecular weight, and Q refers to the specific capacity (mA h g^{-1}). As shown in Figure 4a, at a current density of 0.1 C (1 C = 1830 mA g^{-1}), the COF@D-$Ti_3C_2T_x$ electrode exhibited significantly enhanced performance, delivering an initial discharge/charge capacity of 1030.5/730.2 mA h g^{-1} with a Coulombic efficiency of 70.8%, outperforming pristine COF (962.5/174.3 mA h g^{-1}, 18.1%). During the first 15 cycles, the reversible capacity of the COF@D-$Ti_3C_2T_x$ electrode gradually increased, reaching 401.6 mA h g^{-1} after 300 cycles. This improvement can be attributed to enhanced sodium-ion diffusion kinetics during cycling. The capacity contribution of the COF in the composite was calculated to be 452.5 mA h g^{-1} at 0.1 C after 300 cycles, demonstrating the superior performance of the COF when supported by MXene. The enhanced electrochemical performance of COF@D-$Ti_3C_2T_x$ is attributed to the in situ growth of COF on MXene surfaces, which provides additional active sodium storage sites, facilitates electron and ion transport, and mitigates volume expansion through hydrogen bonding. Furthermore, the cycling capacity of COF@D-$Ti_3C_2T_x$ is comparable to that of many other SIB electrodes reported in the literature (Table S1), highlighting its high reversible capacity and long-term cycling stability.

Rate capabilities, critical indicators of charge transfer and ion diffusion efficiency, were also assessed for the COF, D-$Ti_3C_2T_x$, and COF@D-$Ti_3C_2T_x$ electrodes (Figure 4b). The COF@D-$Ti_3C_2T_x$ electrode demonstrates the highest and most stable specific capacities at various current densities: 409.2, 374.6, 336.3, 298.0, 274.7, 253.9, 229.8, and 191.4 mA h g^{-1} at 0.1 0.2, 0.5, 1, 2, 5, 10, and 20 C, respectively. Remarkably, upon returning to 0.1 C, a capacity of 376.0 mA h g^{-1} can be retained, highlighting efficient Na^+ insertion/extraction during cycling. In contrast, pristine COF exhibits lower rate capacities and reduced Coulombic efficiency under similar conditions. EIS reveals superior conductivity and reduced internal resistance in COF@

https://doi.org/10.1021/acsomega.5c01505
ACS Omega 2025, 10, 16952−16961

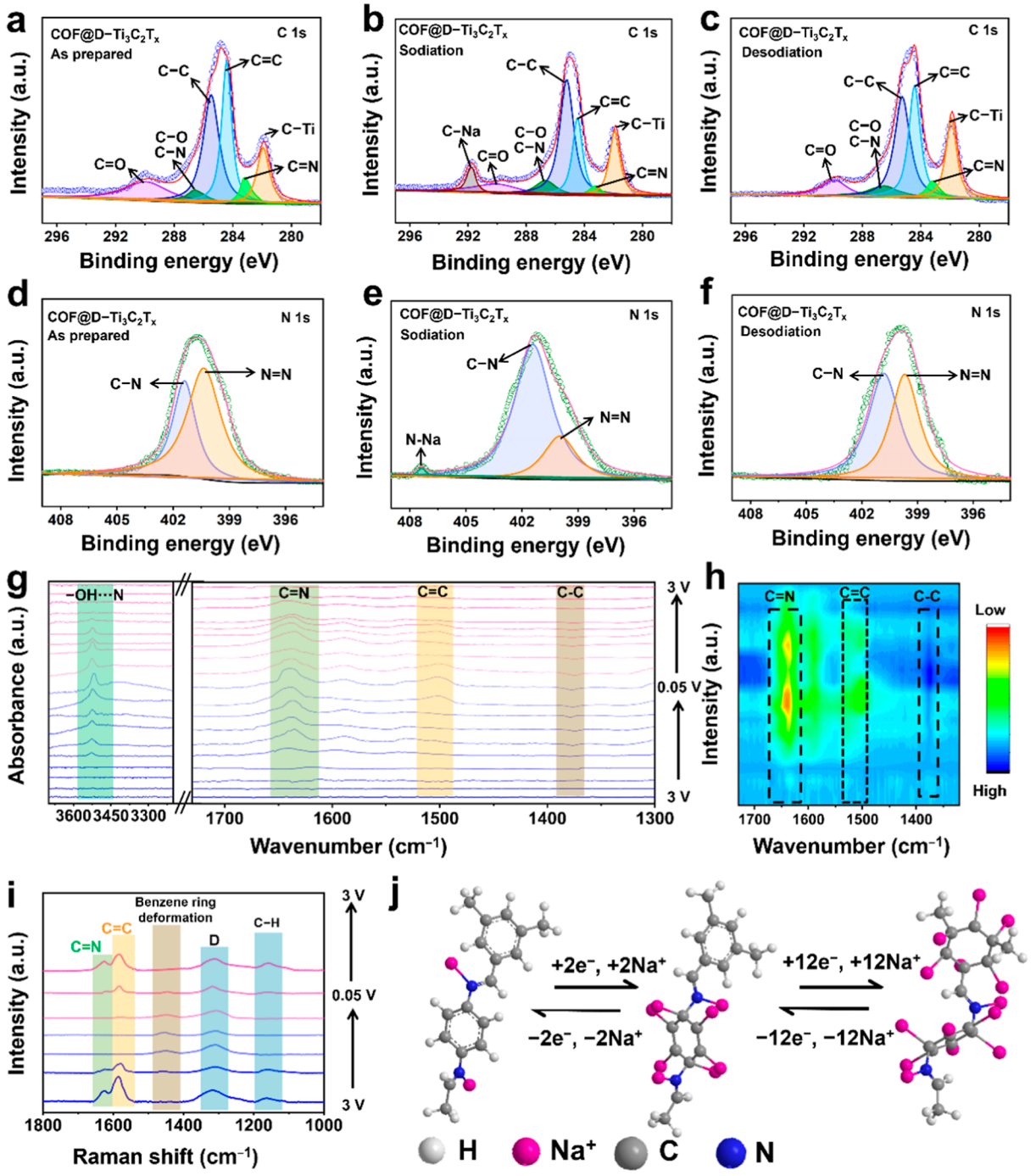

Figure 5. (a–c) C 1s XPS spectra of COF@D-$Ti_3C_2T_x$ during the first fully discharged (sodiation) process to 0.005 V and the first fully charged (desodiation) process to 3.0 V. (d–f) N 1s XPS spectra of COF@D-$Ti_3C_2T_x$ during the sodiation/desodiation process. (g,h) In situ FT-IR characterizations of COF@D-$Ti_3C_2T_x$ during sodiation/desodiation process. (i) In situ Raman characterizations of COF@D-$Ti_3C_2T_x$ during discharge/charge process. (j) Schematic illustration of the sodiation and desodiation process of COF@D-$Ti_3C_2T_x$.

D-$Ti_3C_2T_x$ compared to that of pristine COF (Figure 4c). The charge transfer resistance (R_{ct}) of COF@D-$Ti_3C_2T_x$ (~99 Ω) is significantly lower than that of COF (~230 Ω), correlating with its excellent rate performance and high reversible capacity. After 300 cycles, the charge transfer resistance (R_{ct}) of COF@D-$Ti_3C_2T_x$ dropped to approximately 58 Ω. The COF@D-$Ti_3C_2T_x$ electrodes demonstrated the lowest R_{ct} value among the tested materials, highlighting the advantageous structural design of the composite, which promotes efficient sodium-ion and electron transfer while minimizing diffusion pathways. Notably, the COF@D-$Ti_3C_2T_x$ electrode can maintain stability at ultrahigh current densities (20 C) for 2000 cycles (Figure 4d), showing a superior property in rate performance. Moreover, the morphology of COF@D-$Ti_3C_2T_x$ remained intact after 2000 cycles, indicating that the structure of COF@D-$Ti_3C_2T_x$ is relatively stable during long-term cycling (Figure S5).

To elucidate the sodium storage mechanism, XPS and FT-IR analyses were conducted at various discharging/charging voltages (Figure 5a–f). For the as-prepared COF@D-$Ti_3C_2T_x$, the high-resolution C 1s XPS peaks at 290.1, 286.8,

https://doi.org/10.1021/acsomega.5c01505
ACS Omega 2025, 10, 16952−16961

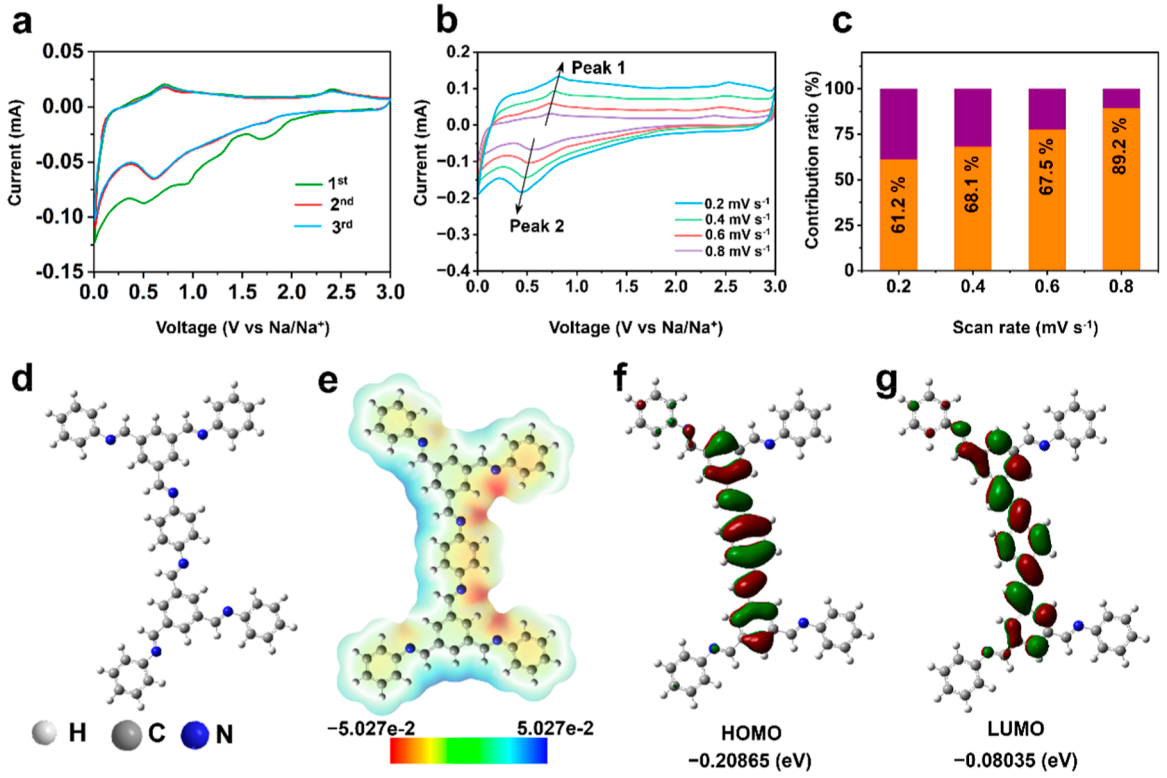

Figure 6. (a) CV curves of the COF@D-$Ti_3C_2T_x$ at 0.1 mV s^{-1}. (b) CV curves at different scan rates ranging from 0.2 to 0.8 mV s^{-1} for COF@D-$Ti_3C_2T_x$. (c) Contribution ratio of capacitive and diffusion-controlled behaviors for COF@D-$Ti_3C_2T_x$. (d) Molecular structure schematic of COF. (e) The molecular electrostatic potential (MESP) of COF. (f) HOMO of COF. (g) LUMO of COF.

285.3, 284.5, 283.3, and 281.9 eV corresponded to C═O, C−N, C−C, C═C, C═N, and C−Ti, respectively.[30,31] After the discharge (sodiation) process, a new peak at 289.6 eV, indexed to C−Na groups, appeared, resulting from the sodiation reaction with the aromatic C═C groups in the benzene rings of COF@D-$Ti_3C_2T_x$.[32] Additionally, the increased peak area proportion of C−C/C═C during sodiation and its decrease during desodiation confirmed the activation of C═C groups for sodium storage.[33] Similarly, the reduced area of C═N and the increased area of C−N during sodiation, followed by the opposite trend during desodiation, indicated the involvement of C═N units in sodium storage. FT-IR tests further revealed the sodium-ion storage mechanism of organic groups in COF@D-$Ti_3C_2T_x$ during cycling (Figure S6). The C═N band exhibited a slight shift after sodiation and recovered after desodiation, confirming the reversible reaction of C═N groups with sodium ions. Additionally, the C═C stretching modes showed weak peaks after sodiation, which recovered after desodiation, indicating a reversible sodium-ion storage mechanism for the C═C groups. These findings collectively demonstrate the synergistic sodium storage behavior of C═N and C═C groups in the COF@D-$Ti_3C_2T_x$.[34,35]

Furthermore, to examine the hydrogen bonding interactions in COF@D-$Ti_3C_2T_x$, in situ FT-IR analysis was conducted (Figure 5g,h). The FT-IR spectra revealed characteristic peaks with an upward trend, suggesting enhanced interactions between the pre-existing functional groups and sodium ions (the initial state was used as a baseline to highlight changes during the cycling process). Specifically, the broad absorption band in the range of 3450−3600 cm^{-1}, corresponding to the −OH stretching vibration from MXene, exhibited a noticeable increase in intensity during discharge, followed by a decrease upon charging. This observation supports the role of hydrogen bond elasticity in alleviating volume expansion during repeated cycling. Additionally, during the discharge phase (3.0 to 0.05 V), the peak intensity at 1627 cm^{-1}, associated with C═N groups, increased, indicating the binding of sodium ions to C═N bonds. Similarly, the bands at 1509−1520 cm^{-1}, attributed to C═C vibrations from the benzene ring skeleton of the COF, also showed an increase in the intensity. These findings imply that both C═N and C═C bonds participate in sodium-ion storage. During the subsequent charging process, the intensities of the C═N and C═C peaks returned to their original levels, signifying the release of sodium ions from these functional groups (C═O and C═C), accompanied by a weakening of the corresponding FT-IR vibrational signals. In addition to the in situ FT-IR analysis, in situ Raman spectroscopy was employed to investigate further the sodium storage mechanism. As depicted in the in situ Raman spectra of COF@D-$Ti_3C_2T_x$ (Figure 5i), distinct peaks at approximately 1627, 1585, 1448, and 1164 cm^{-1} were identified, corresponding to C═N groups, aromatic C═C vibrations from benzene rings, benzene ring deformation, and C−H vibrations from benzene rings, respectively. The peak at ∼1317 cm^{-1} was attributed to the D band of D-$Ti_3C_2T_x$. Notably, the intensity of the C═N peak in the COF@D-$Ti_3C_2T_x$ anode gradually decreased and nearly vanished during the discharge process, followed by gradual recovery upon charging. This behavior is attributed to the reversible interaction between sodium ions and the C═N groups within the COF framework. Similarly, the peak at ∼1585 cm^{-1}, associated with C═C groups, exhibited a significant reduction in intensity during discharge, nearly disappearing at 0.05 V, and then reappeared and intensified after recharging to 3 V. This phenomenon suggests the reversible disruption of C═C

https://doi.org/10.1021/acsomega.5c01505
ACS Omega 2025, 10, 16952−16961

bonds due to sodium-ion insertion and their subsequent restoration upon sodium-ion extraction. Figure 5j shows a schematic illustration of the storage reaction between sodium ions and the COF.

Figure 6a presents the CV of the COF@D-$Ti_3C_2T_x$ and COF electrodes at a scan rate of 0.1 mV s^{-1}. In the first cathodic sweep, a peak located at 1.701 V corresponds to the reaction of sodium ions with C═N. Another peak at 0.956 V can be attributed to the reaction of sodium ions embedded in the benzene ring. And the adjacent peak at 0.504 V corresponds to the generation of the SEI film.[36,37] Two anodic peaks at 0.709 and 2.409 V appear during the desodiation process, corresponding to the desodiation reactions of the benzene ring and C═N, respectively. Moreover, the redox peak at 0.163 and 0.01 V reflects the reversible sodiation−desodiation reactions of network channels and interlayers of COF. In addition, the charging and discharging platform of the COF@D-$Ti_3C_2T_x$ electrode is consistent with the CV peak (Figure S7). In contrast, the CV peaks of the pristine COF are weak, indicating that its benzene ring and C═O groups are less involved in sodium-ion storage due to the insufficient activation (Figure S8).[38,39]

As the excellent cycle performance and rate performance of COF@D-$Ti_3C_2T_x$ draw attention, the relative sodium kinetics in COF@D-$Ti_3C_2T_x$ were investigated. Figure 6b shows the CV of the COF@D-$Ti_3C_2T_x$ electrode at different scan rates from 0.2 to 1.0 mV s^{-1}. It is obvious that the curve shape almost remains unchanged with the increase in scan rates, further indicating the excellent rate performance. The sodium storage mechanism can be revealed by the relationship between the measured current (i) and the scan rate (v) from the CV curves according to the equations as follows: $i = a \times v^b$, $\log i = b \times \log v + \log a$, where v represents the scan rate, i stands for the current, and both a and b are constants ranging from 0.5 to 1.[40,41] Figure S9 reveals the relationship between log i and log v. It can be calculated that the b value is 0.98 and 0.73 for oxidation and reduction states, respectively, suggesting that both conversion reaction and capacitive behavior occur during the discharge/charge processes. Moreover, the capacitive capacity can be further calculated based on the equation: $i(v) = k_1 \cdot v + k_2 \cdot v^{1/2}$, where $i(v)$ represents the measured current at a fixed potential (v), k_1 and k_2 are the adjustable constant parameters, and v represents the scan rate.[42,43] The capacitive contribution to the COF@D-$Ti_3C_2T_x$ electrode increases with the scan rate, indicating the significant existence of the surface absorption mechanism and functional group active spots of the COF@D-$Ti_3C_2T_x$. When the v value increases to 0.8 mV s^{-1}, the capacitive capacity contribution can reach about 89.2% for the COF@D-$Ti_3C_2T_x$ electrode (Figure 6c). These impact factors contribute to the fast charge transfer ability, high capacity, and superior cyclability of the COF@D-$Ti_3C_2T_x$ electrodes. Furthermore, the MESP was simulated to identify the redox-active sites with negative sites in red and positive sites in blue, as depicted in Figure 6d,e. It can be observed that the red (negative) region is mainly concentrated at the C═N groups and benzene rings of the molecule in the COF repeat unit.[44] The distribution of MESP indicates that the negative region located at the C═N groups and benzene rings reacts more easily with the positive Na^+. Moreover, the computed HOMO/LUMO orbital energies of the COF repeat unit are −0.20865/−0.08035 eV (Figure 6f,g). The low HOMO and LUMO energy level difference can promote rapid ion/electron transfer, resulting in improved conductivity and electrochemical properties of COF-based composites in SIBs.[45]

4. CONCLUSIONS

In summary, we have successfully synthesized an imine-based COF and integrated it with MXene through in situ growth to construct an organic−inorganic heterojunction structure. The resulting COF@D-$Ti_3C_2T_x$ composite electrode exhibits outstanding electrochemical performance, attributed to its unique lamellar heterojunction architecture and the activation of sodium storage sites facilitated by the benzene rings and C═N groups. The flexible hydrogen bonds formed between the COF and MXene layers play a critical role in mitigating volume expansion during sodium-ion insertion and extraction, thereby significantly enhancing the long-term cycling stability of the electrode in SIBs. As a result, the COF@D-$Ti_3C_2T_x$ composite electrode delivers a high reversible capacity of 401.6 mA h g^{-1} after 300 cycles at 0.1 C and demonstrates exceptional stability, maintaining consistent performance even at ultrahigh current densities of 20 C for 2000 cycles. This innovative strategy of in situ COF growth on MXene surfaces, mediated by hydrogen bonding, not only maximizes the exposure of active functional groups for sodium storage but also provides a scalable and efficient approach for designing high-performance electrode materials. The findings of this study offer valuable insights into the development of next-generation rechargeable battery technologies, highlighting the potential of organic−inorganic heterojunction structures in advancing energy storage systems.

■ ASSOCIATED CONTENT

Data Availability Statement

The data supporting the findings of this study are available within the article and its Supporting Information. Raw data supporting the findings of this study are available from the corresponding author upon reasonable request.

Supporting Information

The Supporting Information is available free of charge at https://pubs.acs.org/doi/10.1021/acsomega.5c01505.

Digital photograph of COF; XPS survey scan of Ti 2p of COF@D-$Ti_3C_2T_x$; thermal properties of COF, D-$Ti_3C_2T_x$, and COF@D-$Ti_3C_2T_x$ at N_2 atmosphere; TEM images of D-$Ti_3C_2T_x$; SEM images of COF; TEM images of COF@D-$Ti_3C_2T_x$ electrode after 2000 cycles; SEM images of COF@D-$Ti_3C_2T_x$ electrode after 2000 cycles; ex situ FT-IR characterizations of COF@D-$Ti_3C_2T_x$ during sodiation/desodiation process; galvanostatic charge−discharge profiles as recorded at 0.1 C of COF@D-$Ti_3C_2T_x$; CV curves of COF at 0.1 mV s^{-1}; corresponding relationship of Log (i) versus log (v) plots for (c) COF @D-$Ti_3C_2T_x$; and comparison of electrochemical properties (Na-ion batteries) (PDF)

■ AUTHOR INFORMATION

Corresponding Authors

Lu Zheng − *Hubei Institute of Quality Supervision and Inspection Jingzhou Branch, Jingzhou 434000, China*; Email: 13697250792@163.com

Chuanwei Zhi − *Department of Applied Physics, The Hong Kong Polytechnic University, Hong Kong SAR 999077, P. R. China*; orcid.org/0000-0001-7511-0085; Email: chuanwei.zhi@polyu.edu.hk

https://doi.org/10.1021/acsomega.5c01505
ACS Omega 2025, 10, 16952−16961

Chaofei Guo − *Zhejiang Provincial Key Laboratory of Chemical Utilization of Forestry Biomass, Department of Chemistry, Zhejiang A&F University, Hangzhou 311300, China*; orcid.org/0009-0001-2690-1902; Email: chaoguo@zafu.edu.cn

Authors

Xiping Luo − *Zhejiang Provincial Key Laboratory of Chemical Utilization of Forestry Biomass, Department of Chemistry, Zhejiang A&F University, Hangzhou 311300, China*

Mfitumucunguzi Steven − *Zhejiang Provincial Key Laboratory of Chemical Utilization of Forestry Biomass, Department of Chemistry, Zhejiang A&F University, Hangzhou 311300, China*

Zi-Li Feng − *Zhejiang Provincial Key Laboratory of Chemical Utilization of Forestry Biomass, Department of Chemistry, Zhejiang A&F University, Hangzhou 311300, China*

Yu-Xuan Wang − *Zhejiang Provincial Key Laboratory of Chemical Utilization of Forestry Biomass, Department of Chemistry, Zhejiang A&F University, Hangzhou 311300, China*

Xue-Juan Yang − *Zhejiang Provincial Key Laboratory of Chemical Utilization of Forestry Biomass, Department of Chemistry, Zhejiang A&F University, Hangzhou 311300, China*

Complete contact information is available at: https://pubs.acs.org/10.1021/acsomega.5c01505

Author Contributions

[‖]X.L., M.S., and Z.-L.F., contributed equally to this work. X. Luo: conceptualization, methodology, writing-original draft. M. Steven: formal analysis and software; Z. L. Feng: validation and methodology; Y. X. Wang: methodology; X. J. Yang: software; L. Zheng: writing-review and editing; C. W. Zhi: conceptualization and writing-review and editing; C. F. Guo: conceptualization, supervision, and funding acquisition.

Notes

The authors declare no competing financial interest.

■ ACKNOWLEDGMENTS

Financial support from the Central Financial Funds for the Forestry Science and Technology Promotion Application Project in China (no.2023TS01) and the University Research and Development Fund Program (123-203402005101). The authors also would like to thank the Zhejiang Provincial Basic Public Welfare Research Program (LQN25B060011).

■ REFERENCES

(1) Xue, Z. X.; Zhu, D. Y.; Shan, M. H.; Wang, H. K.; Zhang, J.; Cui, G. S.; Hu, Z. X.; Gordon, K. C.; Xu, G. Y.; Zhu, M. F. Functional separator materials of sodium-ion batteries: Grand challenges and industry perspectives. *Nano Today* **2024**, *55*, 102175.

(2) Niitani, K.; Ushiroda, S.; Kuwata, H.; Hozumi, M.; Matsunaga, T.; Nakanishi, S.; Miyazaki, K.; Abe, T.; Nakanishi, S.; Miyazaki, K.; Abe, T. Communication—high-Capacity hard carbons enabled by a sodium carborane solid electrolyte for sodium-ion batteries. *J. Electrochem. Soc.* **2024**, *171*, 010511.

(3) Cai, X. S.; Yue, Y. Y.; Yi, Z.; Liu, J. F.; Sheng, Y. P.; Lu, Y. H. Challenges and industrial perspectives on the development of sodium ion batteries. *Nano Energy* **2024**, *129*, 110052.

(4) He, Z. D.; Huang, Y. J.; Liu, H. X.; Geng, Z. L.; Li, Y. J.; Li, S. M.; Deng, W. T.; Zou, G. Q.; Hou, H. S.; Ji, X. B. Anode materials for fast charging sodium-ion batteries. *Nano Energy* **2024**, *129*, 109996.

(5) Shpalter, D.; Bobyleva, Z. V.; Lakienko, G. P.; Safiullina, A. R.; Jablanovic, A.; Lutsenko, D. S.; Drozhzhin, O. A.; Antipov, E. V. Hard carbon anode materials for hybrid sodium-ion/metal batteries with high energy density. *J. Power Sources* **2024**, *624*, 235547.

(6) Deysher, G.; Oh, J. A. S.; Chen, Y. T.; Sayahpour, B.; Ham, S. Y.; Cheng, D. Y.; Ridley, P.; Cronk, A.; Lin, S. W. H.; Qian, K.; Nguyen, L. H. B.; Jang, J.; Meng, Y. S. Design principles for enabling an anode-free sodium all-solid-state battery. *Nat. Energy* **2024**, *9*, 1161−1172.

(7) Cheng, L. Q.; Yan, X. L.; Yu, J.; Zhang, X. P.; Wang, H. G.; Cui, F. C.; Wang, Y. H. Redox-bipolar covalent organic framework cathode for advanced sodium-organic batteries. *Adv. Mater.* **2024**, *37*, 2411625.

(8) Lee, J.; Lim, H.; Park, J.; Kim, M. S.; Jung, J. W.; Kim, J.; Kim, I. Fluorine-Rich Covalent Organic Framework to Boost Electrochemical Kinetics and Storages of K+ Ions for Potassium-Ion Battery. *Adv. Energy Mater.* **2023**, *13*, 2300442.

(9) Wu, M. M.; Zhao, Y.; Sun, B. Q.; Sun, Z. H.; Li, C. X.; Han, Y.; Xu, L. Q.; Ge, Z.; Ren, Y. X.; Zhang, M. T.; Zhang, Q.; Lu, Y.; Wang, W.; Ma, Y. F.; Chen, Y. S. A 2D Covalent Organic Framework as a High-performance Cathode Material for Lithium-ion Batteries. *Nano Energy* **2020**, *70*, 104498.

(10) Costa, C. M.; Mendez, S. L. Recent Advances on Battery Separators Based on Poly (vinylidene fluoride) and Its Copolymers for Lithium-ion Battery Applications. *Curr. Opin. Electrochem.* **2021**, *29*, 100752.

(11) Guo, C. F.; Han, B.; Sun, W. W.; Cao, Y. N.; Zhang, Y. F.; Wang, Y. Hydrogen-Bonded Organic Framework for High-Performance Lithium/Sodium-Iodine Organic Batteries. *Angew. Chem., Int. Ed.* **2022**, *61*, No. e202213276.

(12) Shea, J. J.; Luo, C. Organic Electrode Materials for Metal Ion Batteries. *CS Appl. Mater. Interfaces* **2020**, *12*, 5361−5380.

(13) Kim, T.; Joo, S. H.; Gong, J.; Choi, S.; Min, J. H.; Kim, Y.; Lee, G.; Lee, E.; Park, S.; Kwak, S. K.; Lee, H. S.; Kim, B. S. Geomimetic Hydrothermal Synthesis of Polyimide-Based Covalent Organic Frameworks. *Angew. Chem., Int. Ed.* **2022**, *61*, No. e202113780.

(14) Sun, W. W.; Tang, X. X.; Yang, Q. S.; Xu, Y.; Wu, F.; Guo, S. Y.; Zhang, Y. F.; Wu, M. H.; Wang, Y. Coordination-Induced Interlinked Covalent and Metal-Organic-Framework Hybrids for Enhanced Lithium Storage. *Adv. Mater.* **2019**, *31*, 1903176.

(15) Luo, Z. Q.; Liu, L. J.; Ning, J. X.; Lei, K. X.; Lu, Y.; Li, F. J.; Chen, J. A Microporous Covalent-Organic Framework with Abundant Accessible Carbonyl Groups for Lithium-Ion Batteries. *Angew. Chem., Int. Ed.* **2018**, *57*, 9443−9446.

(16) Liang, Y.; Tao, Z.; Chen, J. Organic Electrode Materials for Rechargeable Lithium Batteries. *Adv. Energy Mater.* **2012**, *2*, 742−769.

(17) Li, L.; Yin, Y. J.; Hei, J. P.; Wan, X. J.; Li, M. L.; Cui, Y. Molecular Engineering of Aromatic Imides for Organic Secondary Batteries. *Small* **2021**, *17*, 2005752.

(18) Yang, X. B.; Lin, C.; Han, D. D.; Li, G. G.; Huang, C.; Liu, J.; Wu, X.; Zhai, L. P.; Mi, L. W. In situ Construction of Redox-active Covalent Organic Frameworks/carbon Nanotube Composites as Anodes for Lithium-ion Batteries. *J. Mater. Chem. A* **2022**, *10*, 3989−3995.

(19) Wei, C.; Wang, Y.; Zhang, Y.; Tan, L.; Qian, Y.; Tao, Y.; Xiong, S.; Feng, J. Flexible and Stable 3D Lithium Metal Anodes Based on Self-standing MXene/COF Frameworks for High-performance Lithium-sulfur Batteries. *Nano Res.* **2021**, *14*, 3576−3584.

(20) Zou, G.; Zhang, Z.; Guo, J.; Liu, B.; Zhang, Q.; Fernandez, C.; Peng, Q. Synthesis of MXene/Ag Composites for Extraordinary Long Cycle Lifetime Lithium Storage at High Rates. *CS Appl. Mater. Interfaces* **2016**, *8*, 22280−22286.

(21) Lu, C.; Yang, L.; Yan, B.; Sun, L.; Zhang, P.; Zhang, W.; Sun, Z. M. Nitrogen-Doped Ti_3C_2 MXene: Mechanism Investigation and Electrochemical Analysis. *Adv. Funct. Mater.* **2020**, *30*, 2000852.

(22) Ding, Y.; Xiang, S.; Zhi, W.; Gong, S.; He, G.; Wang, T.; Cai, D. Realizing Ultra-Stable Ti_3C_2-MXene in Aqueous Solution via Surface Grafting with Ionomers. *Soft Matter* **2021**, *17*, 4703−4706.

(23) Yang, S.; Yao, J.; Hu, H.; Zeng, Y.; Huang, X.; Liu, T.; Bu, L.; Tian, K.; Lin, Y.; Li, X.; Jiang, S.; Zhou, S.; Li, W.; Bashir, T.; Choi, J. H.; Gao, L.; Zhao, J. Sonication-Induced Electrostatic Assembly of An

$FeCO_3$@Ti_3C_2 Nanocomposite for Robust Lithium Storage. *J. Mater. Chem. A* **2020**, *8*, 23498.
(24) Kim, T.; Joo, S. H.; Gong, J.; Choi, S.; Min, J. H.; Kim, Y.; Lee, G.; Lee, E.; Park, S.; Kwak, S. K.; Lee, H.; et al. Geomimetic Hydrothermal Synthesis of Polyimide-Based Covalent Organic Frameworks. *Angew. Chem., Int. Ed.* **2022**, *134*, No. e202113780.
(25) Yang, X. Y.; Gong, L.; Liu, X. L.; Zhang, P. P.; Li, B. W.; Qi, D. D.; Wang, K.; He, F.; Jiang, J. Z. Mesoporous Polyimide-Linked Covalent Organic Framework with Multiple Redox-Active Sites for High-Performance Cathodic Li Storage. *Angew. Chem., Int. Ed.* **2022**, *61*, No. e202207043.
(26) Wang, C. Y.; Zhang, Z. C.; Zhu, Y. T.; Yang, C. H.; Wu, J. S.; Hu, W. P. 2D Covalent Organic Frameworks: From Synthetic Strategies to Advanced Optical-Electrical-Magnetic Functionalities. *Adv. Mater.* **2022**, *34*, 2102290.
(27) Lei, Z.; Yang, Q.; Xu, Y.; Guo, S.; Sun, W.; Liu, H.; Lv, Li-P.; Zhang, Y.; Wang, Y. Boosting lithium storage in covalent organic framework via activation of 14-electron redox chemistry. *Nat. Commun.* **2018**, *9*, 576.
(28) Yu, Y. L.; Zhang, J.; Shi, Z. J.; Li, Z. Y.; Yan, S. Facile synthesis of $PbBiO_2X/Ti_3C_2$ MXene composites with efficient visible photocatalytic activity. *New J. Chem.* **2023**, *47*, 18315−18324.
(29) Luo, J. M.; Zhang, W. K.; Yuan, H. D.; Jin, C. B.; Zhang, L. Y.; Huang, H.; Liang, C.; Xia, Y.; Zhang, J.; Gan, Y. P.; Tao, X. Y. Pillared Structure Design of MXene with Ultralarge Interlayer Spacing for High-Performance Lithium-Ion Capacitors. *ACS Nano* **2017**, *11*, 2459−2469.
(30) Zhai, L. P.; Li, G. J.; Yang, X. B.; Park, S.; Han, D. D.; Mi, L. W.; Wang, Y. J.; Li, Z. P.; Lee, S. Y. 30 Li^+-Accommodating Covalent Organic Frameworks as Ultralong Cyclable High-Capacity Li-Ion Battery Electrodes. *Adv. Funct. Mater.* **2022**, *32*, 2108798.
(31) Ye, Z.; Liu, Y. J.; Fang, C.; Chen, W.; Ou, M. Y.; Li, L.; Lin, X.; Rao, Z.; Liao, Y. Q.; Zhao, R. R.; Chen, W. L.; Huang, Y. H. Coordination Induced Electron Redistribution to Achieve Highly Reversible Li-ion Insertion Chemistry in Metal-organic Frameworks. *Chem. Commun.* **2020**, *56*, 6424−6427.
(32) Zhao, G. F.; Zhang, Y. H.; Gao, Z. H.; Li, H. N.; Liu, S. M.; Cai, S.; Yang, X. F.; Guo, H.; Sun, X. L. Dual Active Site of the Azo and Carbonyl-Modified Covalent Organic Framework for High-Performance Li Storage. *ACS Energy Lett.* **2020**, *5*, 1022−1031.
(33) Zhang, Y. G.; Wang, J. Q.; Riduan, S. N. Strategies Toward Improving the Performance of Organic Electrodes in Rechargeable Lithium (Sodium) Batteries. *J. Mater. Chem. A* **2016**, *4*, 14902−14914.
(34) Yang, H. Q.; Lee, J.; Cheong, J. Y.; Wang, Y. F.; Duan, G. G.; Hou, H. Q.; Jiang, S. H.; Kim, I. D. Molecular Engineering of Carbonyl Organic Electrodes for Rechargeable Metal-ion Batteries: Fundamentals, Recent Advances, and Challenges. *Energy Environ. Sci.* **2021**, *14*, 4228.
(35) Zhang, X. J.; Zhu, G.; Wang, M.; Li, J. B.; Lu, T.; Pan, L. K. Covalent-organic-frameworks Derived N-doped Porous Carbon Materials as Anode for Superior Long-life Cycling Lithium and Sodium-ion Batteries. *Carbon* **2017**, *116*, 686−694.
(36) Haldar, S.; Kaleeswaran, D.; Rase, D.; Roy, K.; Ogale, S.; Vaidhyanathan, R. Tuning the electronic energy level of covalent organic frameworks for crafting high-rate Na-ion battery anode. *Nanoscale Horiz.* **2020**, *5*, 1264−1273.
(37) Hu, M. M.; Huang, H.; Gao, Q.; Tang, Y.; Luo, Y.; Deng, Y. F.; Zhang, L. Anthraquinone-Based Covalent Organic Framework Nanosheets with Ordered Porous Structures for Highly Reversible Sodium Storage. *Energy Fuels* **2021**, *35*, 1851−1858.
(38) Shehab, M. K.; Weeraratne, K. S.; Huang, T.; Lao, K. U.; El-Kaderi, H. M. Exceptional Sodium-Ion Storage by an Aza-Covalent Organic Framework for High Energy and Power Density Sodium-Ion Batteries. *ACS Appl. Mater. Interfaces* **2021**, *13* (13), 15083−15091.
(39) Xie, M. G.; Li, C. G.; Ren, S. Y.; Ma, Y.; Chen, X. B.; Fan, X. F.; Han, Y.; Shi, Z.; Feng, S. H. Ultrafine Sb nanoparticles in situ confined in covalent organic frameworks for high-performance sodium-ion battery anodes. *J. Mater. Chem. A* **2022**, *10*, 15089−15100.
(40) Cao, Y. N.; Sun, W. W.; Guo, C. F.; Zheng, L.; Yao, M. Y.; Wang, Y. Rational Construction of Yolk−Shell Bimetal-Modified Quinonyl-Rich Covalent Organic Polymers with Ultralong Lithium-Storage Mechanism. *ACS Nano* **2022**, *16* (6), 9830−9842.
(41) Guo, C. F.; Liu, T. C.; Wang, Z. Z.; Wang, Y. X.; Steven, M.; Luo, Y. H.; Luo, X. P.; Wang, Y. Regulating the Spin-State of Cobalt in Three-Dimensional Covalent Organic Frameworks for High-Performance Sodium-Iodine Rechargeable Batteries. *Angew. Chem., Int. Ed.* **2025**, *64*, No. e202415759.
(42) Wu, M. M.; Zhao, Y.; Zhao, R. Q.; Zhu, J.; Liu, J.; Zhang, Y. M.; Li, C. X.; Ma, Y. F.; Zhang, H. T.; Chen, Y. S. Chemical Design for Both Molecular and Morphology Optimization toward High-Performance Lithium-Ion Batteries Cathode Material Based on Covalent Organic Framework. *Adv. Funct. Mater.* **2022**, *32*, 2107703.
(43) Guo, Z.; Dong, G.; Zhang, M.; Gao, M.; Shao, L.; Chen, M.; Liu, H.; Ni, M.; Cao, D.; Zhu, K. Sulfur-Decorated $Ti_3C_2T_X$ MXene for High-Performance Sodium/Potassium-Ion Batteries. *Chem.−Asian J.* **2023**, *18*, No. e202300336.
(44) Guo, C. F.; Gao, Y.; Li, S. Q.; Wang, Y. X.; Yang, X. J.; Zhi, C. W.; Zhang, H.; Zhu, Y. F.; Chen, S. Q.; Chou, S. L.; Dou, S. X.; Xiao, Y.; Luo, X. P. Chemical-Stabilized Aldehyde-Tuned Hydrogen-Bonded Organic Frameworks for Long-Cycle and High-Rate Sodium-Ion Organic Batteries. *Adv. Funct. Mater.* **2024**, *34*, 2314851.
(45) Cao, Y. N.; Sun, Y.; Guo, C. F.; Sun, W. W.; Wu, Y.; Xu, Y.; Liu, T. C.; Wang, Y. Dendritic sp Carbon-Conjugated Benzothiadiazole-Based Polymers with Synergistic Multi-Active Groups for High-Performance Lithium Organic Batteries. *Angew. Chem., Int. Ed.* **2023**, *63*, No. e202316208.

https://doi.org/10.1021/acsomega.5c01505
ACS Omega 2025, 10, 16952−16961